CrossMark

JFM RAPIDS
journals.cambridge.org/rapids

Electric-field-induced transitions from spherical to discocyte and lens-shaped drops

Brayden W. Wagoner[1], Petia M. Vlahovska[2], Michael T. Harris[1] and Osman A. Basaran[1],†

[1]Davidson School of Chemical Engineering, Purdue University, West Lafayette, IN 47907, USA

[2]Department of Engineering Sciences and Applied Mathematics, Northwestern University, Evanston, IL 60208, USA

When a poorly conducting drop that is surrounded by a more conducting exterior fluid is subjected to an electric field, the drop can deform into an oblate shape at low field strengths. Such drops become unstable at high field strengths and display two types of dynamics, dimpling and equatorial streaming, the physics of which is currently not understood. If the drop is more viscous, dimples form and grow at the poles of the drop and eventually the discocyte-shaped drop breaks up to form a torus. If the exterior fluid is more viscous, the drop deforms into a lens and sheds rings from the equator that subsequently break into a number of smaller droplets. A theoretical explanation as to why dimple- and lens-shaped drops occur, and the mechanisms for the onset of these instabilities, are provided by determining steady-state solutions by simulation and inferring their stability from bifurcation analysis. For large drop viscosities, electric shear stress is shown to play a dominant role and to result in dimpling. For small drop viscosities, equatorial normal stresses (electric, hydrodynamic and capillary) become unbounded and lead to the lens shape.

Key words: drops, electrohydrodynamic effects

1. Introduction

Coupling between electric fields $\tilde{E}$ and hydrodynamics – electrohydrodynamics (EHD) – has interested scientists since Gilbert reported that static electricity generated from rubbed amber could 'attract' water (Gilbert 1958). The birth of the modern science of EHD, however, can be traced to three papers: Rayleigh's discovery (Rayleigh 1882; Tsamopoulos, Akylas & Brown 1985) that highly charged drops can become unstable, Taylor's analysis (Taylor 1964) of equilibria and stability of conducting drops subjected

† Email address for correspondence: obasaran@purdue.edu

to $\tilde{E}$ that showed that strong fields can deform drops into prolate shapes with conical tips along $\tilde{E}$ (Miksis 1981; Basaran & Scriven 1990), and Taylor's discovery (Taylor 1966) that imperfectly conducting or leaky dielectric (LD) (Melcher & Taylor 1969) drops can be deformed parallel (prolate) or perpendicular (oblate) to $\tilde{E}$. These papers and experiments (Zeleny 1917) on jet emission or EHD tipstreaming (Collins *et al.* 2008, 2013; Oddershede & Nagel 2000; Burton & Taborek 2011) from the conical ends of pendant drops – electrospraying (Barrero & Loscertales 2007; Fernández de La Mora 2007; Ganán-Calvo *et al.* 2018) – laid the foundation for widely used applications. Examples – all involving highly conducting drops surrounded by a gas and prolate deformations – include electrospray ionization mass spectrometry, electrospinning, and printing of cells (Fenn *et al.* 1989; Feng 2002; Jayasinghe, Qureshi & Eagles 2006; Reneker & Yarin 2008).

Cases where both phases are viscous fluids (Marín *et al.* 2007; Vlahovska 2019) and drops exhibit both prolate and oblate deformations have been receiving increasing attention (Feng & Scott 1996; Lac & Homsy 2007; Yariv & Rhodes 2013; Das & Saintillan 2017*a*,*b*) due to their wide-ranging importance (Harris, Sisson & Basaran 1992; Zhang, Basaran & Wham 1995; Baygents, Rivette & Stone 1998; Eow *et al.* 2001; Marín *et al.* 2007; Bird *et al.* 2009; Ristenpart *et al.* 2009). Recent experiments (Brosseau & Vlahovska 2017) have uncovered a previously unknown type of EHD *equatorial streaming* instability. Here, a poorly conducting drop is dispersed in a more conducting exterior liquid (figure 1*a*). A weak $\tilde{E}$ drives the drop to adopt an oblate shape, in accord with theory (Taylor 1966; Melcher & Taylor 1969). As shown in Brosseau & Vlahovska (2017) and Vlahovska (2019), such drops become unstable as $|\tilde{E}|$ increases. Although it is known that the nature of the instabilities that arise with oblate drops depends on the ratio of fluid viscosities, the physical mechanisms for their onset have heretofore remained elusive and are uncovered from theory in this paper. We demonstrate that if the drop is more viscous, electric shear stress plays a dominant role and a strong $\tilde{E}$ creates a dimple at each pole of the oblate drop that resembles a discocyte or biconcave disk (figure 1*b*). These dimples grow and the drop eventually ruptures to form a torus. This mode of breakup is called dimpling. If the exterior phase is more viscous, we show that a strong $\tilde{E}$ drives the oblate drop into a biconvex lens (figure 1*c*) because equatorial normal stresses – electric, hydrodynamic and capillary – become unbounded as $|\tilde{E}|$ increases. Interestingly, Torza, Cox & Mason (1971) have briefly mentioned in a couple of sentences the occurrence of lenses in their experiments, albeit without further discussion. In the recent experiments, rings of fluid are then emitted from the lens-shaped drop's equator which subsequently break into droplets (Brosseau & Vlahovska 2017; Vlahovska 2019). This mode of breakup is called equatorial streaming.

We examine the physics for the onset of these two instabilities and their dependence on viscosity ratio by determining steady-state solutions of the governing equations by simulation. We adopt this approach as it is currently unclear whether dimpling and equatorial streaming instabilities arise due to the loss of stability of a steady-state solution at a turning (limit) point or a bifurcation point (Iooss & Joseph 2012) with respect to applied field strength. We demonstrate that both instabilities arise at turning points when the applied field strength reaches a critical value. First, we take advantage of experimental results (Brosseau & Vlahovska 2017) to judiciously probe portions of the relevant parameter space that have been overlooked in previous computational studies (Feng & Scott 1996; Feng 1999; Lac & Homsy 2007). Second, contrary to some recent studies, we do not approximate solutions using expansions based on spheroidal harmonics (Bentenitis & Krause 2005; Zabarankin 2013). Lens-shaped drops have not been reported
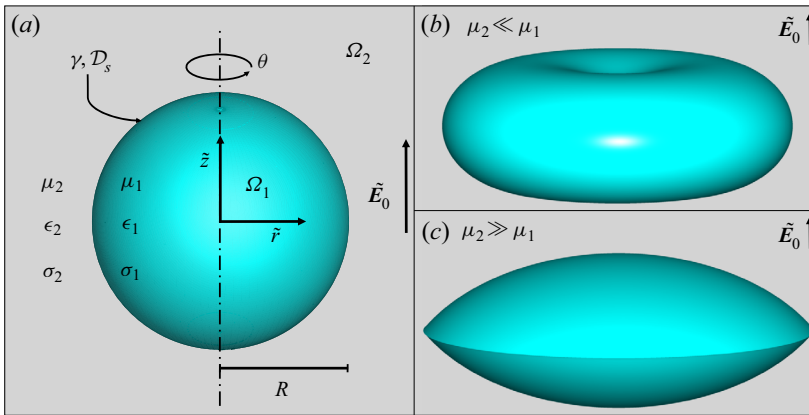
FIGURE 1. (*a*) A spherical drop subjected to an electric field. At large field strengths, the ratio of outer to inner fluid viscosity (μ_2/μ_1) determines the drop's fate: (*b*) discocyte and (*c*) lens. Here and in all of the figures that can be found in the remainder of this paper, all drop shapes that are shown are those that have been obtained from simulations.

in these previous studies relying on the use of expansions based on spheroidal harmonics. Moreover, to date, when the exterior fluid is more viscous, only stable steady-states have been computed numerically (Zabarankin 2013; Lanauze, Walker & Khair 2015). Hence, for the first time, we resolve theoretically the onset of the instability that arises when the exterior fluid is more viscous, in agreement with the equatorial streaming instability experimentally observed in Brosseau & Vlahovska (2017).

The article is organized as follows. Section 2 describes the mathematical formulation of the problem. A brief summary of the numerical method used in the simulations is then provided in § 3. As it is imperative to impress upon the reader an intuitive understanding of drop deformation caused by an applied electric field, a quick overview is presented in § 4 on the physics of electric-field-induced deformation in drops of LD fluids as opposed to drops of perfectly conducting or perfectly insulating fluids. Simulation results are then presented and discussed in § 5. The paper concludes in § 6 with concluding remarks and a summary of possible directions for further study.

2. Problem statement

The system (figure 1) consists of two neutrally buoyant phases ($i = 1, 2$; $i = 1$, drop; $i = 2$, exterior), each of which is an incompressible, Newtonian, LD (Melcher & Taylor 1969; Saville 1997) fluid of constant physical properties (viscosity μ_i, permittivity ϵ_i and conductivity σ_i) undergoing Stokes flow. In the absence of electric field, $\tilde{E}_i = \mathbf{0}$, the drop is a sphere of radius R. It bears no net charge. The interface separating the two fluids has constant surface tension γ as well as diffusivity for charge $\mathcal{D}_s$. We use a cylindrical coordinate system ($\tilde{r}, \theta, \tilde{z}$) based at the centre of the sphere and where these variables stand for the radial, angular and axial coordinates. The drop is subjected to an electric field $\tilde{\mathbf{E}}_0 = \tilde{E}_0 \mathbf{e}_z$ of uniform strength $\tilde{E}_0$ far from the drop ($\mathbf{e}_z$: unit vector in $\tilde{z}$ direction). The problem is non-dimensionalized using as characteristic scales R for length, $t_c \equiv \mu_1 R/\gamma$ for time (t_c: visco-capillary time), γ/R for hydrodynamic stress, $\tilde{E}_0$ for electric field, $\epsilon_2 \tilde{E}_0$ for surface charge density and $\epsilon_2 \tilde{E}_0^2$ for electric stress. Aside from the three dimensionless

parameter ratios $\chi \equiv \sigma_1/\sigma_2$, $\kappa \equiv \epsilon_1/\epsilon_2$ and $\lambda \equiv \mu_2/\mu_1$, three other dimensionless groups arise: (i) electric Bond number $N_E \equiv \epsilon_2 \tilde{E}_0^2 R / 2\gamma$ (the ratio of electric to surface tension force), (ii) dimensionless charge relaxation time in either phase, $\alpha_i \equiv (\epsilon_i/\sigma_i)/t_c$ ($i = 1$ or 2, $\alpha_2/\alpha_1 = \chi/\kappa$), and (iii) Péclet number $Pe \equiv (R^2/\mathcal{D}_s)/t_c = \gamma R/\mu_1 \mathcal{D}_s$ (the ratio of the time scale for charge diffusion on the surface $R^2/\mathcal{D}_s$ and the visco-capillary time t_c). In what follows, variables without tildes are the dimensionless counterparts of those with tildes.

The steady-state deformation of the drop and the flow field and electric potential Φ_i (where $E_i = -\nabla \Phi_i$) inside (Ω_1) and outside (Ω_2) the drop are governed by the axisymmetric continuity, Stokes and Laplace equations:

$$\nabla \cdot v_i = 0, \quad \nabla \cdot T_i^H = 0, \quad \nabla^2 \Phi_i = 0 \quad \text{in } \Omega_i, \qquad (2.1a\text{--}c)$$

where v_i is the velocity, $T_i^H \equiv -p_i I + (\mu_i/\mu_1)[(\nabla v)_i + (\nabla v)_i^T]$ the hydrodynamic stress, and p_i the pressure.

Along the drop surface S_f, the flow and electric field in each phase are coupled through the traction condition

$$n \cdot [T_i^H + 2N_E T_i^E]_1^2 = 2\mathcal{H} n, \qquad (2.2)$$

where $T_i^E \equiv (\epsilon_i/\epsilon_2)(E_i E_i - E_i^2 I/2)$ is the electric (Maxwell) stress tensor (Melcher & Taylor [1969](#)), n the outward-pointing unit normal and $2\mathcal{H}$ twice the mean curvature. The notation $[x]_1^2$ denotes the jump in x in going from phase 1 to phase 2. Along S_f, the kinematic boundary condition $n \cdot v_1 = n \cdot v_2 = 0$ (Kistler & Scriven [1983](#); Christodoulou & Scriven [1992](#); Deen [1998](#)) and no slip $t \cdot [v_i]_1^2 = 0$, where t denotes the unit tangent to S_f in the cross-sectional plane, are imposed. Additionally along S_f, the tangential component of the electric field is continuous, $t \cdot [E_i]_1^2 = 0$, but the normal component of the electric displacement suffers a discontinuity given by the surface charge density, $q \equiv n \cdot [(\epsilon_i/\epsilon_2)E_i]_1^2$. In the LD model (Melcher & Taylor [1969](#)), bulk density of charge is zero but surface charge density on S_f is governed by a transport equation which, under steady-state conditions, is given by

$$\nabla_s \cdot (q v) - Pe^{-1} \nabla_s^2 q = \frac{1}{\alpha_2} \left(\frac{\sigma_1}{\sigma_2} n \cdot E_1 - n \cdot E_2 \right) \qquad (2.3)$$

on S_f. Here, v is the velocity and E_1 and E_2 are electric fields at S_f, and ∇_s is the surface gradient. In this equation, the terms on the left side represent surface charge transport by convection and diffusion, and the source-like terms on the right represent charge transport from each phase to S_f by Ohmic conduction. In the limit where charge transport by diffusion and charge transport by convection are negligible (Taylor [1966](#); Melcher & Taylor [1969](#)), this equation reduces to the continuity of the normal component of the electric current, $n \cdot [(\sigma_i/\sigma_2)E_i]_1^2 = 0$.

3. Simulations and numerical method

The governing equations are solved by numerical simulation using a finite-element-based algorithm over one quadrant of the *rz*-plane ($r, z \geq 0$) subject to symmetry conditions along $r = 0$ (axis of symmetry) and $z = 0$ (plane of symmetry). Far from the drop's centre-of-mass, the electric potential is set to asymptotically approach that of a uniform

field and the flow field is taken to be stress-free. Similar versions of the algorithm employed here have been used for solving equilibrium (Basaran & Scriven 1990; Sambath & Basaran 2014), steady-state (Basaran & Scriven 1988) and transient (Collins *et al.* 2013) problems in EHD. The algorithm relies on elliptic mesh generation (Christodoulou & Scriven 1992) and continuation with adaptive parameterization (Abbott 1978) to determine steady-state solution families (Feng & Basaran 1994), and automatically detects points where changes of stability occur (Brown & Scriven 1980; Ungar & Brown 1982; Yamaguchi, Chang & Brown 1984). In all simulations, $Pe = 10^3$ (Collins *et al.* 2008, 2013). We note that all simulation results presented in the paper are insensitive to changes in *Pe* provided that $Pe \gg 1$, as shown in the appendix.

4. Physics of drop deformation

Interfacial flows and drop deformations observed in LD fluids are made possible by the electric shear stress at S_f, $[T_{nt}^E]_1^2 \equiv \boldsymbol{n} \cdot [\boldsymbol{T}_i^E]_1^2 \cdot \boldsymbol{t} = qE_t$ where $E_t \equiv \boldsymbol{t} \cdot \boldsymbol{E}_i$. Following Taylor (1966), we focus first on the situation in the absence of charge convection and diffusion. The electric normal stress at S_f can then be expressed as $[T_{nn}^E]_1^2 \equiv \boldsymbol{n} \cdot [\boldsymbol{T}_i^E]_1^2 \cdot \boldsymbol{n} = [E_{1,n}^2(\chi^2 - \kappa) + E_t^2(\kappa - 1)]/2$ where $E_{1,n} \equiv \boldsymbol{n} \cdot \boldsymbol{E}_1$, and the charge density is given by $q = E_{1,n}(\chi - \kappa)$. When the drop has a smaller permittivity and is of relatively even lesser conductivity than the surrounding fluid, $\chi/\kappa = (\epsilon_2/\sigma_2)(\sigma_1/\epsilon_1) < 1$ and $\kappa = \epsilon_1/\epsilon_2 < 1$, electric normal stress $[T_{nn}^E]_1^2$ is compressive, i.e. acts inward, but is not necessarily uniform, on S_f. Moreover, both q and $[T_{nt}^E]_1^2$ are negative (positive) on the top (bottom) half of the drop, and the flow along S_f is therefore from the drop's poles to its equator.

We now illustrate that electric normal stress alone is insufficient to determine the drop's fate when the applied field is sufficiently weak so that a spherical drop suffers negligible deformation. If the drop were spherical, the field inside it would be uniform, $\boldsymbol{E}_1 = 3\boldsymbol{e}_z/(\chi + 2)$. The electric normal stress at the poles is then given by $E_1^2(\chi^2 - \kappa)/2$, and that at the equator is $E_1^2(\kappa - 1)/2$. When $\chi \to 0$, in this spherical state, it follows that the difference between the electric normal stress at the pole and at the equator, $\Delta_E^P([T_{nn}^E]_1^2)$, is given by $E_1^2(-2\kappa + 1)/2$. Thus, if $\kappa = \epsilon_1/\epsilon_2 > 1/2$, then electric normal stress at the pole is more compressive than that at the equator ($\Delta_E^P([T_{nn}^E]_1^2) < 0$), and the converse is true for $\kappa < 1/2$. If electric normal stress is more (less) compressive at the pole than at the equator, the drop is more likely to adopt an oblate (prolate) shape at finite field strengths. However, non-uniformity in electric normal stress is just one way of driving deformation in LD drops, whereas it is the sole way of doing so when the drop is either a perfect conductor or perfect insulator and the exterior a perfect insulator (Taylor 1964). A more exact analysis (Melcher & Taylor 1969) including electric shear stress shows that when $\chi \to 0$ and $\lambda \to \infty$, transition between prolate and oblate deformations occurs at $\kappa = 5/16 = 0.3125$. Thus, as was first shown by Taylor (1966) and Smith & Melcher (1967), considering electric normal stress alone is in general insufficient, because it overlooks the role played by electric tangential and hydrodynamic normal stresses that may arise on account of flows induced by $[T_{nt}^E]_1^2$.

To illustrate the crucial importance of electric shear stress, we examine next by simulations situations in which $\epsilon_1/\epsilon_2 = 1/2$ when $\chi \ll 1$ (as in the experiments of Brosseau & Vlahovska (2017)). In this situation, electric normal stress is not only equal at the poles and the equator but is in fact uniform everywhere on the surface of a spherical drop. Since a uniform stress causes no deformation, the resulting drop deformation at low field strengths is driven by the action of electric shear stress. As the role of viscosity ratio
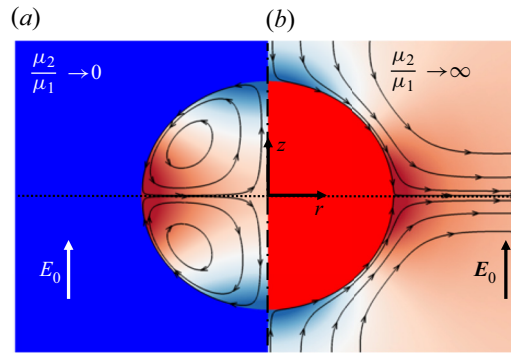
FIGURE 2. Steady-state streamlines (*a*) inside and (*b*) outside, and pressure distributions inside/outside a drop in the limit of vanishingly small applied electric field strength for two systems in which the drop is much less conducting and has a lower permittivity than the exterior. Here and in the next two figures, $(\epsilon_2/\sigma_2)(\sigma_1/\epsilon_1) = 0.02$, $\epsilon_1/\epsilon_2 = 1/2$ and $\alpha_2 = 2 \times 10^{-4}$ (therefore, $\alpha_1 = 10^{-2}$). Panels (*a*) and (*b*) correspond, respectively, to the limits in which exterior viscosity and interior viscosity tend to zero. In both (*a*) and (*b*), warmer (cooler) or red (blue) colour implies higher (lower) pressure.

in the dimpling and equatorial streaming instabilities has heretofore been incompletely understood, it is reasonable to anticipate that the goal of elucidating the mechanisms for the onset of these instabilities would be best accomplished by considering two limits in which the drop is either much more or much less viscous than the exterior fluid, viz. $\mu_2/\mu_1 \ll 1$ or $\mu_2/\mu_1 \gg 1$. In both limits, the direction of flow on S_f does not change, as it is induced purely by electric shear stress, which depends solely on electrical properties.

5. Results and discussion

5.1. *Limit of* $\mu_2/\mu_1 \ll 1$

When $\mu_2/\mu_1 \to 0$, the exterior fluid behaves as if it were a passive gas that simply exerts a constant pressure on the drop, and the physics can be appreciated by focusing on the flow in Ω_1. Here, electric tangential stress at S_f drives fluid from the pole(s), $(r, z) = (0, \pm z|_{pole})$, to the equator, $(r, z) = (r|_{eq}, 0)$. Because of mass conservation, the pressure at the equator then has to rise compared to that at the pole(s) for the fluid to return to the pole(s). Thus, a recirculating eddy arises as shown in figure 2(*a*), and the resulting flow resembles those in the lid-driven cavity and Taylor pump (Melcher & Taylor 1969; Basaran & Scriven 1988). Because the pressure rises at the equator and falls at the poles, the curvature increases at the equator and decreases at the poles: the drop bulges out at the equator and flattens at the poles.

To better quantify drop deformation, figure 3(*a*) shows in a bifurcation diagram the variation of the steady-state deformation of the drop $D \equiv (z|_{pole} - r|_{eq})/(z|_{pole} + r|_{eq})$ with electric Bond number N_E for a system in which the drop is less conducting and has a lower permittivity but is much more viscous than the outer fluid. Figure 3(*b*) shows the variation with D of the difference between the value at the pole and that at the equator of all three normal stresses. In order to better discern the role of electric normal stress $[T_{nn}^E]_1^2$, two sets of solutions are shown in that figure: one set where electric normal stress in (2.2) is operative and another where this term has been turned off, i.e. $[T_{nn}^E]_1^2 = 0$ (Collins *et al.* 2008; Kamat *et al.* 2018). When electric normal stress is turned off, it can no longer induce
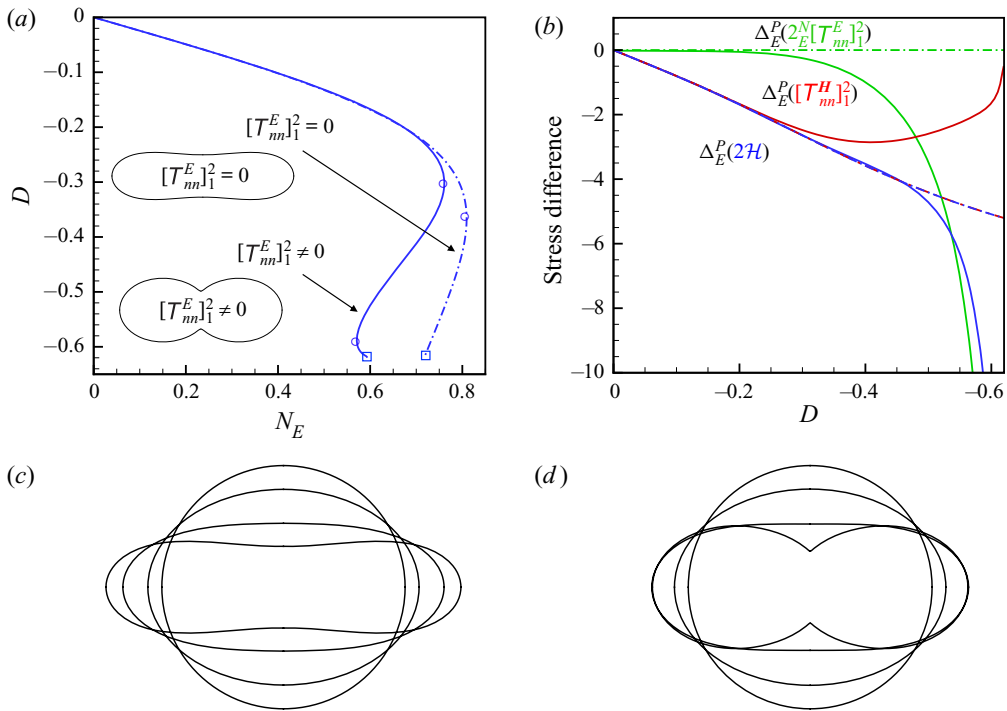
FIGURE 3. Bifurcation diagram, stresses and drop shapes for steady-state solutions when the drop is much less conducting and has a lower permittivity but is much more viscous than the outer fluid ($\mu_2/\mu_1 = 0.02$). Variation of (*a*) deformation D with electric Bond number N_E for shape families of dimpled shapes and (*b*) difference between the value at the pole and the equator of all three normal stresses (hydrodynamic (red), electric (green), and capillary (blue)) with D. Solutions depicted in (*a*) and (*b*) here and in the next figure have been obtained from simulations in which electric normal stress $[T_{nn}^E]_1^2$ is on (solid curves) and in its absence (dash-dotted curves). In panel (*a*) here and in the next figure, circles indicate locations of turning points and shape insets show drop profiles when $[T_{nn}^E]_1^2 = 0$ or $\neq 0$ at points marked by a square symbol. (*c*) Sequence of drop shapes obtained from simulations along the shape family for which electric normal stress is turned off, $[T_{nn}^E]_1^2 = 0$, and (*d*) that for which this stress is operative, $[T_{nn}^E]_1^2 \neq 0$. In (*c*), the values of (N_E, D) for which these shapes are shown are $(0, 0)$, $(0.583, -0.162)$, $(0.799, -0.431)$ and $(0.714, -0.626)$. In (*d*), the values of (N_E, D) for which these shapes are shown are $(0, 0)$, $(0.581, -0.160)$, $(0.685, -0.429)$ and $(0.595, -0.625)$.

and hence contribute to the deformation of the drop. By comparing solutions obtained when electric normal stress is acting and when it is absent, its role in determining the fate of the drop can be made plain.

As can be seen in figure 3(*b*), electric tangential stress (as described earlier) causes hydrodynamic normal stress to rise at the equator and fall at the poles ($\Delta_E^P([T_{nn}^H]_1^2) < 0$). For small deformations ($|D| < 0.2$), simulations with electric normal stress turned on show that there is virtually no electric normal stress difference between the pole and the equator. Hence, capillary normal stress (capillary pressure) must balance hydrodynamic normal stress ($\Delta_E^P(2\mathcal{H}) < 0$). As field strength or N_E increases, electric shear stress and hence the concomitant flow strengthen, driving the hydrodynamic and capillary normal stresses to further rise at the equator and fall at the poles, and thereby to cause drop deformation to grow. This trend persists until the drop becomes flattened at the poles and

the curvature there equals zero. Any further increase in electric shear stress and disparity in hydrodynamic normal stress between the equator and the pole(s) then causes the curvature at the pole(s) to change sign and hence causes a dimple(s) to form. Hence, we say that steady-state solutions that lie along either solution branch – with normal stress on and with it turned off – in the bifurcation diagram of figure 3(*a*) are members of the shape family (families) of dimpled shapes (discocytes). Figure 3(*a*) shows that as N_E increases from zero, a turning point arises when $(N_E, D) = (N_E^*, D^*)$ along the solution families. It is shown in standard books on bifurcation theory (Glendinning 1994; Seydel 2009; Iooss & Joseph 2012) that starting with a solution that is known to be stable, solutions are linearly stable as a control parameter is varied until a turning point is reached. Here, the known stable solution corresponds to a spherical drop ($D = 0$) in the absence of electric field or when the electrical Bond number N_E – the control parameter – equals 0. Therefore, as N_E is increased, the solutions along a solution family or solution branch are stable until a turning point (N_E^*, D^*) is reached. Whereas solutions for values of $0 < N_E^*, 0 \leq |D| < |D^*|$ are stable, those beyond the turning point(s) are unstable (Brown & Scriven 1980; Ungar & Brown 1982; Yamaguchi *et al.* 1984; Feng & Basaran 1994; Glendinning 1994; Seydel 2009; Iooss & Joseph 2012). Comparison of the shape insets in figure 3(*a*) reveals that dimpling and instability occur even in the absence of electric normal stress and that electric normal stress acts to accentuate the dimple(s). Figure 3(*a*) further shows that the solution family with $[T_{nn}^E]_1^2$ turned on exhibits a second turning point as $|D|$ increases, a point that is returned to below. Sequences of drop shapes of increasing deformation along both shape families are shown in figures 3(*c*) and 3(*d*).

5.2. *Limit of $\mu_2/\mu_1 \gg 1$*

When $\mu_2/\mu_1 \to \infty$, the drop behaves like a void in which pressure is constant. In Ω_2, electric tangential stress on S_f drives flow from the pole(s) to the equator just outside the drop. Thus, a pressure gradient arises along the symmetry axis where fluid far from the drop flows toward it such that pressure is low and normal viscous stress is compressive at the drop's pole(s), $(r, z) = (0, \pm z|_{pole})$, and a pressure gradient also arises at the plane of symmetry where fluid is driven from the equatorial mid-plane toward infinity such that pressure is high and normal viscous stress is extensional at the drop's equator, $(r, z) = (r|_{eq}, 0)$ (figure 2*b*). Unlike the dimpling case, here the pressure difference between the pole and equator causes a prolate drop deformation while the (larger) viscous normal stress difference drives an oblate deformation.

Figure 4(*a*) shows D as a function of N_E for a system in which the drop is less conducting and has a lower permittivity but is also much less viscous than the outer fluid. Figure 4(*b*) shows the difference between the value at the pole and that at the equator of all three normal stresses as a function of D. Once again, solutions depicted in figure 4 have been obtained both with electric normal stress on and with it turned off. In the absence of electric normal stress, $[T_{nn}^E]_1^2 = 0$, drop deformation is driven by hydrodynamic normal stress and balanced by capillary stress (figure 4*b* dash-dotted curves). In this case, the shape family reaches a turning point when $N_E \approx 1$: drops before the turning point are stable whereas those after it are unstable. However, the steady-state shapes (figure 4*c*) do not resemble the characteristic lens-like shapes that lead to equatorial streaming. This shape family is referred to as the family of spheroids. By contrast and as shown in figure 4(*a*), when $[T_{nn}^E]_1^2 \neq 0$, electric normal stress acts to arrest the increase of D with N_E. This is made plain by figure 4(*b*) which reveals that electric normal stress at the equator is more compressive than its counterpart(s) at the pole(s), thereby decreasing the extent of deformation. While deformation on the drop-scale (measured by D) is arrested, interface
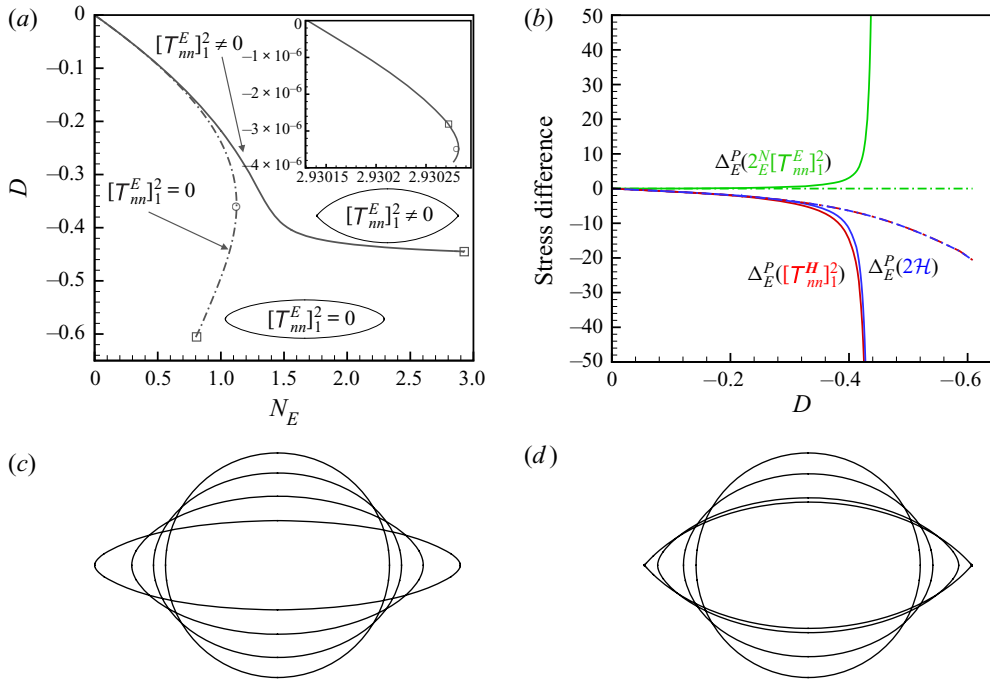
FIGURE 4. Same as figure 3 but where the drop is much less viscous than the outer fluid ($\mu_2/\mu_1 = 50$). Variation of (a) D with N_E for shape families of spheroids ($[T^E_{nn}]^2_1 = 0$) and lenses ($[T^E_{nn}]^2_1 \neq 0$) and (b) difference between the value at the pole and the equator of all three normal stresses (hydrodynamic (red), electric (green), and capillary (blue)) with D. The upper right inset in (a) is a blow-up of the main figure where the turning point is located when $[T^E_{nn}]^2_1 \neq 0$, i.e. the lens family. In the inset, values of N_E are shown along the horizontal axis as in the main figure, but the vertical axis has been shifted so that the values shown correspond to $D + 0.444815$ for clarity. (c) Sequence of drop shapes obtained from simulations along the family of spheroids (for which electric normal stress is turned off, $[T^E_{nn}]^2_1 = 0$) and (d) that for the lens family (for which this stress is operative, $[T^E_{nn}]^2_1 \neq 0$). In (c), the values of (N_E, D) for which these shapes are shown are $(0, 0)$, $(0.731, -0.148)$, $(1.122, -0.374)$ and $(0.797, -0.608)$. In (d), the values of (N_E, D) for which these shapes are shown are $(0, 0)$, $(0.774, -0.155)$, $(1.442, -0.382)$ and $(2.930, -0.445)$.

deformation at the local scale at the equator (measured by interface curvature or $|2\mathcal{H}|$) is enhanced. At the equator, under the action of ever increasing (normal) electric force, the three stresses comprising compressive electric normal stress, extensional hydrodynamic normal stress and capillary stress due to equatorial curvature not only compete but appear to grow without bound, giving rise to the solution family of lens-like shapes – the lens family – whose highly deformed members (figure 4d) are precursors to equatorial streaming. Thus, for the first time, we theoretically observe the onset of this instability (inset, figure 4a) in agreement with experimental results (Brosseau & Vlahovska 2017).

6. Conclusions

When the exterior fluid's conductivity is much larger than the drop's, members of shape families of drops become increasingly deformed as electric field strength or electric Bond

number N_E rises and lose stability at turning points. Highly deformed members of these families are discocytes when the drop is much more viscous than its exterior, $\mu_2/\mu_1 \ll 1$, and lenses when $\mu_2/\mu_1 \gg 1$, in accord with experiments (Brosseau & Vlahovska 2017; Vlahovska 2019). Through careful scrutiny of the stresses acting to deform a drop, it has been conclusively shown that the instability that arises in the former case is caused by a drastically different mechanism than the latter one. It has been shown that dimpling occurs purely as a result of electric tangential stress: dimple-shaped drops arise and become unstable at a turning point in N_E with and without electric normal stress. However, lens-shaped drops arise as a result of electric normal stress and do not occur in its absence. Theoretical analysis of the rim of the lens, similar to those in studies of the conic cusp singularity in EHD tipstreaming from the Taylor cones at the tips of prolate drops (Zubarev 2001; Collins *et al.* 2008), is so far lacking, but is underway.

While the geometry of the lens and that of the Taylor cone is similar, the analogy between these two phenomena ends there. A Taylor cone (Taylor 1964) exists under electrohydrostatic conditions, i.e. in the absence of flow, in which electric and capillary normal stresses balance. Unlike Taylor cones, lenses form only in the presence of flow. Consequently, viscous, electric and capillary normal stresses are in balance in the case of lenses. Another crucial difference between the two cases is that in Taylor cones, electric and capillary normal stresses act in opposite directions at the apex of the cone, whereas in lenses they act in the same direction, i.e. they are compressional or act inward, at the equator.

It was heretofore unknown whether equatorial streaming could be predicted using the LD equations. It has been demonstrated here that these equations do give rise to unstable solutions. Once destabilized, lens-shaped drops emit equatorial sheets, as has been shown in a preliminary computational study in which the unstable steady-state shapes beyond the turning point along the lens family are used as initial conditions in transient simulations (Wagoner *et al.* 2019). Developing a thorough understanding of the transient dynamics that occurs when drops become unstable and succumb to dimpling ($\mu_2/\mu_1 \ll 1$) or equatorial streaming ($\mu_2/\mu_1 \gg 1$) is of great theoretical importance and is underway. It is noteworthy that interface shapes in the vicinity of the axis of symmetry, i.e. near $r = 0$, both above and below the plane of symmetry, appear conical for drops that are members of the family of dimpled shapes (discocytes). When these conical interfaces approach each other after the onset of the dimpling instability, the dynamics that ensues should follow that reported in Bird *et al.* (2009). Thus, whether the cone angle is larger or smaller than the critical cone angle reported in Bird *et al.* (2009) would determine whether the outcome is dimple merger or recoil. Investigating which of the two outcomes arises once a dimple-shaped drop has destabilized is left as an open problem for future computational studies on the transient dynamics of unstable discocytes.

According to the results presented in § 5.1, two turning points arise along the family of discocytes (figure 3). Thus, while there is a loss of stability at the first turning point, the family regains its stability at the second turning point (Glendinning 1994; Seydel 2009). Hence, the family of discocytes exhibits hysteresis in the parameter space of drop deformation D versus electric Bond number N_E. Yet another worthy goal of future studies should be whether such hysteretic response, which has been widely encountered in past studies of equilibria and dynamics of drops subjected to electric and/or magnetic fields (Basaran & Wohlhuter 1992; DePaoli *et al.* 1995), can be observed in laboratory experiments.

Acknowledgements

Declaration of interests

The authors report no conflict of interest.

Appendix. Effect of Péclet number *Pe*

In the main part of the paper, a value of $Pe = 10^3$ has been used to obtain all simulation results. In this appendix, we examine the effect of *Pe* on the discocyte and lens families.

The value of the Péclet number of 10^3 used in this paper is based on the experiments of Brosseau & Vlahovska (2017) and on certain reasonable assumptions that we had to make to arrive at a ballpark value of this dimensionless group. In the experiments of Brosseau & Vlahovska (2017), the drop fluid was silicone oil and the exterior fluid was castor oil. The value of the surface or interfacial tension was $\gamma = 0.0045$ N m^{-1} for all drop–exterior fluid combinations, and the typical radius of the undeformed drop was $R = 0.001$ m. Using $\mu_1 = 0.0138$ Pa s (a typical value of the drop viscosity in the experiments) and the definition of *Pe*, it follows that $\mathcal{D}_s = 3.26 \times 10^{-4} \, Pe^{-1}$ m^2 s^{-1}. While it is hard to measure surface charge diffusion coefficients $\mathcal{D}_s$, and Brosseau & Vlahovska (2017) (and others) do not report values of $\mathcal{D}_s$, based on reported values of other surface diffusion coefficients (e.g. for surfactant transport) we expect $\mathcal{D}_s$ to be of the order of 10^{-6} to 10^{-8} m^2 s^{-1}. We therefore made the reasonable choice to use the intermediate value of $Pe = 10^3$ in the main part of the paper. However, since the surface diffusivity and hence the Péclet number can vary by a factor of about one hundred, we examine below the effect of varying *Pe* by several orders of magnitude.

Figure 5 shows the variation of the steady-state deformation *D* as a function of the electric Bond number N_E for three Péclet numbers ($Pe = 10^2$, 10^3 and 10^4) when the drop is (*a*) much more viscous ($\lambda = 0.02$) and (*b*) much less viscous ($\lambda = 50$) than the exterior fluid. In both panels (*a*) and (*b*), the drop is less conducting and has a lower permittivity than the surrounding fluid. As discussed in the article, when the drop is more viscous than the exterior fluid, tangential electric stress and the flows induced by this stress deform the drop into a dimpled or discocyte-like shape (figure 5*a*). When the drop is less viscous than the exterior fluid, however, equatorial normal stresses grow rapidly with deformation and give rise to a lens-like shape (figure 5*b*). Figure 5 makes plain that the existence of both shape families – discocytes and lenses – and the occurrence of turning points along each shape family where stable solutions lose stability as N_E and/or *D* increase(s) are independent of *Pe*.

For the family of dimpled shapes (figure 5*a*), varying *Pe* insignificantly affects the solution family, the values of the critical Bond number N_E^* and critical deformation D^* at the turning point(s), and the drop shape even at the largest value of the steady-state drop deformation *D* shown in the figure. Indeed, the solution families and the drop shapes shown as insets in figure 5(*a*) lie on top of each other and are virtually indistinguishable.

For the lens family (figure 5*b*), varying *Pe* insignificantly affects the solution families over most of the parameter space. The value of the critical electric Bond number for instability, N_E^*, increases slightly with *Pe*. However, the value of the critical deformation
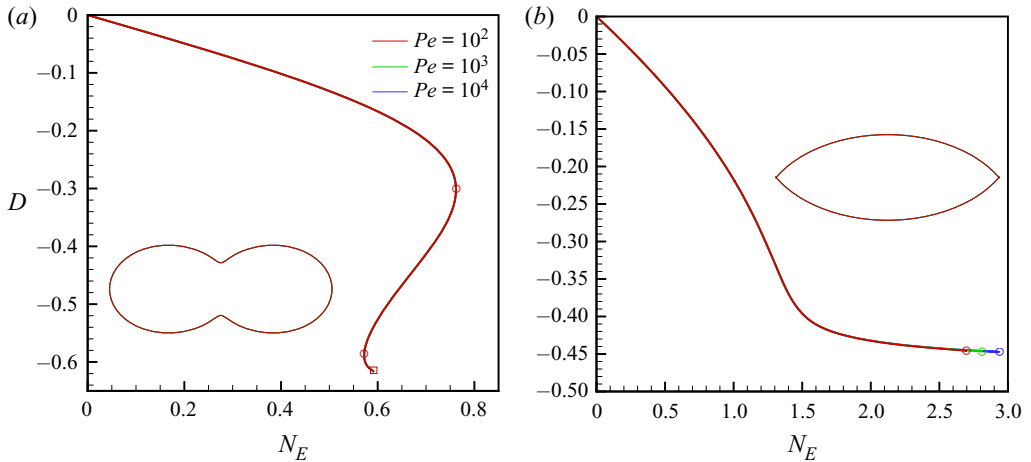
FIGURE 5. Bifurcation diagram of steady-state solutions showing the variation of drop deformation D with electric Bond number N_E when the drop is much less conducting and has a lower permittivity than the surrounding fluid, with $(\epsilon_2/\sigma_2)(\sigma_1/\epsilon_1) = 0.02$, $\epsilon_1/\epsilon_2 = 1/2$ and $\alpha_2 = 2 \times 10^{-3}$ (therefore, $\alpha_1 = 10^{-1}$). (*a*) Drop is much more viscous than the outer fluid ($\lambda = 0.02$): family of dimpled shapes (discocytes). (*b*) Drop is much less viscous than the outer fluid ($\lambda = 50$): lens family. In both (*a*) and (*b*), simulation results are shown for $Pe = 10^2$ (red curve), $Pe = 10^3$ (green curve) and $Pe = 10^4$ (blue curve). In both (*a*) and (*b*), circles denote the locations of the turning points. The shape insets show the drop profile at the point marked by a square symbol in (*a*) and at the turning points in (*b*). Solution curves or shape families and drop shapes obtained at different Pe mostly overlap and hence appear as single curves in the figure.

D^* is virtually unchanged, and drop shapes at the turning points obtained for different values of Pe overlap so that they are virtually indistinguishable (see inset to figure 5*b*). The variation of N_E^* with Pe is currently under further investigation, as it may have promising applications. Specifically, comparison of the critical electric Bond number obtained from simulations and experiments can provide a new method for determining the surface diffusivity of charge ($\mathcal{D}_S$), which, like other surface properties, is often challenging to measure.

In summary, the two distinct instabilities that arise when the drop is much more viscous than the surroundings – dimpling – and the drop is much less viscous than the surroundings – lens formation – are unaffected when Péclet number is varied. The mechanisms of drop deformation and instability also remain the same as Pe is varied. In particular, when lenses form, the rim of the lens is corner-like with a semi-angle of approximately $\pi/4$ regardless of the value of Pe. Reassuringly, a similar corner-like geometry and angle are observed at the incipience of instability in the experiments of Brosseau & Vlahovska (2017).

References

ABBOTT, J. P. 1978 An efficient algorithm for the determination of certain bifurcation points. *J. Comput. Appl. Maths* **4** (1), 19–27.

BARRERO, A. & LOSCERTALES, I. G. 2007 Micro-and nanoparticles via capillary flows. *Annu. Rev. Fluid Mech.* **39**, 89–106.

904 R4-12

BASARAN, O. A. & SCRIVEN, L. E. 1988 The Taylor pump: viscous-free surface flow driven by electric shear stress. *Chem. Engng Commun.* **67** (1), 259–273.

BASARAN, O. A. & SCRIVEN, L. E. 1990 Axisymmetric shapes and stability of pendant and sessile drops in an electric field. *J. Colloid Interface Sci.* **140** (1), 10–30.

BASARAN, O. A. & WOHLHUTER, F. K. 1992 Effect of nonlinear polarization on shapes and stability of pendant and sessile drops in an electric (magnetic) field. *J. Fluid Mech.* **244**, 1–16.

BAYGENTS, J. C., RIVETTE, N. J. & STONE, H. A. 1998 Electrohydrodynamic deformation and interaction of drop pairs. *J. Fluid Mech.* **368**, 359–375.

BENTENITIS, N. & KRAUSE, S. 2005 Droplet deformation in DC electric fields: the extended leaky dielectric model. *Langmuir* **21** (14), 6194–6209.

BIRD, J. C., RISTENPART, W. D., BELMONTE, A. & STONE, H. A. 2009 Critical angle for electrically driven coalescence of two conical droplets. *Phys. Rev. Lett.* **103** (16), 164502.

BROSSEAU, Q. & VLAHOVSKA, P. M. 2017 Streaming from the equator of a drop in an external electric field. *Phys. Rev. Lett.* **119** (3), 034501.

BROWN, R. A. & SCRIVEN, L. E. 1980 The shapes and stability of captive rotating drops. *Phil. Trans. R. Soc. Lond.* A **297** (1429), 51–79.

BURTON, J. C. & TABOREK, P. 2011 Simulations of coulombic fission of charged inviscid drops. *Phys. Rev. Lett.* **106** (14), 144501.

CHRISTODOULOU, K. N. & SCRIVEN, L. E. 1992 Discretization of free surface flows and other moving boundary problems. *J. Comput. Phys.* **99** (1), 39–55.

COLLINS, R. T., JONES, J. J., HARRIS, M. T. & BASARAN, O. A. 2008 Electrohydrodynamic tip streaming and emission of charged drops from liquid cones. *Nat. Phys.* **4** (2), 149.

COLLINS, R. T., SAMBATH, K., HARRIS, M. T. & BASARAN, O. A. 2013 Universal scaling laws for the disintegration of electrified drops. *Proc. Natl Acad. Sci.* **110** (13), 4905–4910.

DAS, D. & SAINTILLAN, D. 2017*a* Electrohydrodynamics of viscous drops in strong electric fields: numerical simulations. *J. Fluid Mech.* **829**, 127–152.

DAS, D. & SAINTILLAN, D. 2017*b* A nonlinear small-deformation theory for transient droplet electrohydrodynamics. *J. Fluid Mech.* **810**, 225–253.

DEEN, W. M. 1998 Analysis of transport phenomena. Oxford University Press.

DEPAOLI, D. W., FENG, J. Q., BASARAN, O. A. & SCOTT, T. C. 1995 Hysteresis in forced oscillations of pendant drops. *Phys. Fluids* **7** (6), 1181–1183.

EOW, J. S., GHADIRI, M., SHARIF, A. O. & WILLIAMS, T. J. 2001 Electrostatic enhancement of coalescence of water droplets in oil: a review of the current understanding. *Chem. Engng J.* **84** (3), 173–192.

FENG, J. Q. 1999 Electrohydrodynamic behaviour of a drop subjected to a steady uniform electric field at finite electric Reynolds number. *Proc. R. Soc. Lond.* A **455** (1986), 2245–2269.

FENG, J. J. 2002 The stretching of an electrified non-Newtonian jet: a model for electrospinning. *Phys. Fluids* **14** (11), 3912–3926.

FENG, J. Q. & BASARAN, O. A. 1994 Shear flow over a translationally symmetric cylindrical bubble pinned on a slot in a plane wall. *J. Fluid Mech.* **275**, 351–378.

FENG, J. Q. & SCOTT, T. C. 1996 A computational analysis of electrohydrodynamics of a leaky dielectric drop in an electric field. *J. Fluid Mech.* **311**, 289–326.

FENN, J. B., MANN, M., MENG, C. K., WONG, S. F. & WHITEHOUSE, C. M. 1989 Electrospray ionization for mass spectrometry of large biomolecules. *Science* **246** (4926), 64–71.

FERNÁNDEZ DE LA MORA, J. 2007 The fluid dynamics of Taylor cones. *Annu. Rev. Fluid Mech.* **39**, 217–243.

GANÁN-CALVO, A. M., LÓPEZ-HERRERA, J. M., HERRADA, M. A., RAMOS, A. & MONTANERO, J. M. 2018 Review on the physics of electrospray: from electrokinetics to the operating conditions of single and coaxial Taylor cone-jets, and AC electrospray. *J. Aero. Sci.* **125**, 32–56.

GILBERT, W. 1958 *De Magnete*. Courier Corporation.

GLENDINNING, P. 1994 *Stability, Instability and Chaos: An Introduction to the Theory of Nonlinear Differential Equations*, vol. 11. Cambridge University Press.

HARRIS, M. T., SISSON, W. G. & BASARAN, O. A. 1992 Computation, visualization, and chemistry of electric field-enhanced production of ceramic precursor powders. *MRS Online Proc. Library Arch.* **271**, 945–950.

IOOSS, G. & JOSEPH, D. D. 2012 *Elementary Stability and Bifurcation Theory*. Springer Science & Business Media.

JAYASINGHE, S. N., QURESHI, A. N. & EAGLES, P. A. M. 2006 Electrohydrodynamic jet processing: an advanced electric-field-driven jetting phenomenon for processing living cells. *Small* **2** (2), 216–219.

KAMAT, P. M., WAGONER, B. W., THETE, S. S. & BASARAN, O. A. 2018 Role of Marangoni stress during breakup of surfactant-covered liquid threads: reduced rates of thinning and microthread cascades. *Phys. Rev. Fluids* **3** (4), 043602.

KISTLER, S. F. & SCRIVEN, L. E. 1983 Coating flows. In *Computational Analysis of Polymer Processing* (ed. J. R. A. Pearson & S. M. Richardson), pp. 243–299. Springer.

LAC, E. & HOMSY, G. M. 2007 Axisymmetric deformation and stability of a viscous drop in a steady electric field. *J. Fluid Mech.* **590**, 239–264.

LANAUZE, J. A., WALKER, L. M. & KHAIR, A. S. 2015 Nonlinear electrohydrodynamics of slightly deformed oblate drops. *J. Fluid Mech.* **774**, 245–266.

MARÍN, A. G., LOSCERTALES, I. G., MARQUEZ, M. & BARRERO, A. 2007 Simple and double emulsions via coaxial jet electrosprays. *Phys. Rev. Lett.* **98** (1), 014502.

MELCHER, J. R. & TAYLOR, G. I. 1969 Electrohydrodynamics: a review of the role of interfacial shear stresses. *Annu. Rev. Fluid Mech.* **1** (1), 111–146.

MIKSIS, M. J. 1981 Shape of a drop in an electric field. *Phys. Fluids* **24** (11), 1967–1972.

ODDERSHEDE, L. & NAGEL, S. R. 2000 Singularity during the onset of an electrohydrodynamic spout. *Phys. Rev. Lett.* **85** (6), 1234.

RAYLEIGH, LORD 1882 On the equilibrium of liquid conducting masses charged with electricity. *Phil. Mag.* **14** (87), 184–186.

RENEKER, D. H. & YARIN, A. L. 2008 Electrospinning jets and polymer nanofibers. *Polymer* **49** (10), 2387–2425.

RISTENPART, W. D., BIRD, J. C., BELMONTE, A., DOLLAR, F. & STONE, H. A. 2009 Non-coalescence of oppositely charged drops. *Nature* **461** (7262), 377–380.

SAMBATH, K. & BASARAN, O. A. 2014 Electrohydrostatics of capillary switches. *AIChE J.* **60** (4), 1451–1459.

SAVILLE, D. A. 1997 Electrohydrodynamics: the Taylor–Melcher leaky dielectric model. *Annu. Rev. Fluid Mech.* **29** (1), 27–64.

SEYDEL, R. 2009 *Practical Bifurcation and Stability Analysis*, vol. 5. Springer Science & Business Media.

SMITH, C. V. & MELCHER, J. R. 1967 Electrohydrodynamically induced spatially periodic cellular Stokes-flow. *Phys. Fluids* **10** (11), 2315–2322.

TAYLOR, G. I. 1964 Disintegration of water drops in an electric field. *Proc. R. Soc. Lond.* A **280** (1382), 383–397.

TAYLOR, G. I. 1966 Studies in electrohydrodynamics. I. The circulation produced in a drop by an electric field. *Proc. R. Soc. Lond.* A **291** (1425), 159–166.

TORZA, S., COX, R. G. & MASON, S. G. 1971 Electrohydrodynamic deformation and bursts of liquid drops. *Phil. Trans. R. Soc. Lond.* A **269** (1198), 295–319.

TSAMOPOULOS, J. A., AKYLAS, T. R. & BROWN, R. A. 1985 Dynamics of charged drop break-up. *Proc. R. Soc. Lond.* A **401** (1820), 67–88.

UNGAR, L. H. & BROWN, R. A. 1982 The dependence of the shape and stability of captive rotating drops on multiple parameters. *Phil. Trans. R. Soc. Lond.* A **306** (1493), 347–370.

VLAHOVSKA, P. M. 2019 Electrohydrodynamics of drops and vesicles. *Annu. Rev. Fluid Mech.* **51**, 305–330.

WAGONER, B. W., ANTHONY, C. R., VLAHOVSKA, P. M., HARRIS, M. T. & BASARAN, O. A. 2019 Electrohydrodynamic equatorial streaming. *Bull. Am. Phys. Soc.* **64**, B23.001.

YAMAGUCHI, Y., CHANG, C. J. & BROWN, R. A. 1984 Multiple buoyancy-driven flows in a vertical cylinder heated from below. *Phil. Trans. R. Soc. Lond.* A **312** (1523), 519–552.

YARIV, E. & RHODES, D. 2013 Electrohydrodynamic drop deformation by strong electric fields: slender-body analysis. *SIAM J. Appl. Maths* **73** (6), 2143–2161.

ZABARANKIN, M. 2013 A liquid spheroidal drop in a viscous incompressible fluid under a steady electric field. *SIAM J. Appl. Maths* **73** (2), 677–699.

ZELENY, J. 1917 Instability of electrified liquid surfaces. *Phys. Rev.* **10** (1), 1.

ZHANG, X., BASARAN, O. A. & WHAM, R. M. 1995 Theoretical prediction of electric field-enhanced coalescence of spherical drops. *AIChE J.* **41** (7), 1629–1639.

ZUBAREV, N. M. 2001 Formation of conic cusps at the surface of liquid metal in electric field. *J. Expl Theor. Phys. Lett.* **73** (10), 544–548.